Charge Ordering in a 2D Manganite, $Pr_{0.25}Ca_{1.75}MnO_4$

C. Autret,[†,‡] R. Retoux,[†] M. Hervieu*,[†] and B. Raveau[†]

Laboratoire Crismat, UMR 6508 associée au CNRS, ISMRA, 6 boulevard du Maréchal Juin, 14050 Caen Cedex, France, and Laboratoire Léon Brillouin, CEA-CNRS, Centres d'études de Saclay, 91191 Gif-sur-Yvette Cedex, France

Received June 20, 2001. Revised Manuscript Received September 7, 2001

The structural study of the manganite $Pr_{0.25}Ca_{1.75}MnO_4$, $n = 1$ member of the Ruddlesden−Popper (RP) family, has been carried out using high-resolution electron microscopy and neutron powder diffraction. At room temperature, the K_2NiF_4-type structure is characterized by its ability to microtwine and form perovskite-like "pancake" defects, coherent with the matrix. The most important point concerns the appearance at low temperature of an incommensurate structure with a modulation vector $\vec{q} \approx 0.28\vec{c}^*$, never observed to date in these 2D manganites. The reconstruction of the reciprocal space, using electron diffraction technique, evidences *Cmca(00γ)s00* as the superspace group. The transition temperature, $T_{CO} = 275$ K, explains the anomalies of the $\rho(T)$ and M(T) curves, characterized by an increase of resistivity and appearance of antiferromagnetic fluctuations below this temperature.

Introduction

Renewed interest in colossal magnetoresistance (CMR) effects has stimulated numerous studies on manganites with the perovskite structure, $Ln_{1-x}Ae_xMnO_3$ (Ln = lanthanides, Ae = divalent alkaline earth element). The application of magnetic fields causes magnetic transitions and also CMR effects and structural transitions. CMR properties originate from double-exchange (DE) interactions between Mn^{3+} and Mn^{4+} species,[1−4] so that the electrical resistivity of oxides containing Mn in a mixed oxidation state ($Mn^{3+/4+}$) can decrease dramatically in an applied field. In recent studies of colossal magnetoresistance manganites, it has been recognized that the correlations between spin, charge, and orbital degrees of freedom play important roles in their physical properties.[5−7]

These perovskite-type manganites exhibit a 3D character. To modify and understand these properties, much attention has been focused on low-dimensional derivatives, the Ruddlesden−Popper (RP) phases $(Ln, A)_{n+1}Mn_nO_{3n+1}$. The existence of charge ordering below 220 K in the $n = 1$ member of this series and its influence upon the resistive and magnetic transitions were shown for the first time by Moritomo et al.[8] for $La_{0.5}Sr_{1.5}MnO_4$ and confirmed by Sternlieb et al.[9] from elastic neutron scattering measurements. The first clear evidence of orbital ordering in this 2D manganite was then given by Murakami et al.,[10] showing that orbital ordering and charge ordering occur simultaneously, above the spin-ordering temperature. Investigation of the $n = 1$ member, $Ln_{1-x}Ca_{1+x}MnO_4$, was also made for other lanthanides.[11−12] In any case, the "**1**−**1**" ordering, which consists of one Mn^{3+} row of octahedra alternating with one Mn^{4+} row, in each octahedral layer, is the only charge-ordered state that has been observed to date in these $n = 1$ member of the RP series. In the present paper, a complete structural study of the $n = 1$ member, $Pr_{0.25}Ca_{1.75}MnO_4$, is performed, using electron diffraction (ED), high-resolution electron microscopy (HREM), and neutron powder diffraction (NPD). We show that this calcium-rich manganite exhibits a new type of charge and orbital ordering, corresponding to a "**1**−**3**" ordering below $T_{CO} = 275$ K, in connection with a charge of slope of $\rho(T)$ at this temperature, and an abrupt decrease of the magnetization below T_{CO}. Extended defects and their close neighboring, which may influence the physical properties of this oxide, are studied.

Experimental Section

The sample $Pr_{0.25}Ca_{1.75}MnO_4$ was prepared by solid-state reaction from stoichiometric amounts of CaO, Pr_6O_{11}, and MnO_2. The mixture was first heated twice 24 h at 1000 °C. The powder was reground, pressed into pellets (1 ton/cm^2), sintered at 1300 °C for 24 h, and then fired at 1550 °C for 12 h. Finally, the sample was cooled to 800 °C and quenched to room temperature.

The oxygen content has been determined from neutron powder diffraction (NPD) refinements and confirmed by iodometric titration to the O_4 stoichiometric value per unit.

* To whom correspondence should be addressed.
† Laboratoire Crismat.
‡ Laboratoire Léon Brillouin.

(1) Zener, C. *Phys. Rev.* **1951**, *82*, 403.
(2) Anderson, P. W.; Hasegawa, H. *Phys. Rev.* **1955**, *100*, 67.
(3) de Gennes, P.-G. *Phys. Rev.* **1960**, *118*, 141
(4) Jonker, G. H.; Santen, J. H. *Physica* **1950**, *16*, 337
(5) Urushiba, A.; Moritomo, Y.; Arima, T.; Asamitsu, A.; Kido, G.; Tokura, Y. *Phys. Rev. B* **1995**, *51*, 14103.
(6) Moritomo, Y.; Asamitsu, A.; Tokura, Y. *Phys. Rev. B* **1997**, *56*, 12190.
(7) Zhong, F.; Wang, Z. D. *Phys. Rev. B* **2000**, *61*, 3192.
(8) Moritomo, Y.; Tomioka, Y.; Asamitsu, A.; Tokura, Y.; Matsui, Y. *Phys. Rev. B* **1995**, *51*, 3297.
(9) Sternlieb, B. J.; Hill, J. P.; Wildgruber, U. C.; Luke, G. M.; Nachumi, B.; Moritomo, Y.; Tokura, Y. *Phys. Rev. Lett.* **1996**, *76*, 2169.
(10) Murakami, Y.; Kawada, H.; Tanaka, M.; Avima, T.; Moritomo, Y.; Tokura, Y. *Phys. Rev. Lett.* **1998**, *80*, 1932.
(11) Moritomo, Y.; Nakamura, A.; Mori, S.; Yamamoto, N.; Ohoyama, K.; Ohashi, M. *Phys. Rev. B* **1997**, *56*, 14879.
(12) Maignan, A.; Martin, C.; Van Tendeloo, G.; Hervieu, M.; Raveau, B. *J. Mater. Chem.* **1998**, *8*, 2411.

10.1021/cm010381v CCC: $20.00
Published on Web 11/08/2001

Table 1. Cell Parameters, Atomic Coordinates Deduced from Neutron Diffraction Refinements: $R_p = 12\%$, $R_{wp} = 11.6\%$, $\chi_2 = 12.6$, $R_{bragg} = 5.04\%$

atoms[a]	site	*x*	*y*	*z*
Ca, Pr	8f	0	0.3563 (1)	−0.006 (1)
Mn	4a	0	0	0
O1	8f	0	0.1630 (1)	−0.009 (1)
O2	8e	0.25	−0.0002 (1)	0.25

[a] $a = 5.3025$ (3) Å, $b = 11.8934$ (2) Å, $c = 5.2995$ (2) Å, and $V = 334.22$ (2) Å^3.

The sample for electron microscopy study was prepared by smoothly crushing the crystallites in alcohol. The small flakes were deposited on a holey carbon film supported by a copper grid. Preliminary electron diffraction (ED) and EDS characterization was carried out at room temperature with a JEOL 200CX electron microscope. The ED study versus temperature was carried out with a JEOL 2010 electron microscope. The HREM study was carried out with a 200kV TOPCON 002B microscope (point resolution of 1.8 Å, Cs = 0.4 mm). Theoretical images were calculated for different focus values and crystal thickness using the multislice method with the Mac Tempas software. The three electron microscopes are equipped with energy dispersive spectroscopy (EDS) analyzers.

The neutron diffraction patterns were recorded at room temperature on the 3T2 diffractometer of the Laboratory Leon Brillouin (LLB, Saclay) with $\lambda = 1.2251$ Å (angular range $6° < 2\theta < 125.6°$, step 0.02). Structural refinements were performed with the Rietveld method using the Fullprof program.[13]

A Quantum Design Superconducting Quantum Interference Device (SQUID) magnetometer was used to record the magnetization data under a 3000 G magnetic field. The data were collected during cooling and warming.

The transport properties were investigated with a Quantum Design Physical Property Measuring System (PPMS). Resistivity data were recorded from 300 to 5 K under 0 and 7 T magnetic field.

Structure Determination at Room Temperature. The XRPD pattern and electron diffraction study evidenced a single-phased sample. Energy dispersive spectroscopy (EDS) analyses confirm the great homogeneity of the sample and that the cationic composition is close to the nominal one, $Pr_{0.25}Ca_{1.75}$-Mn.

The reconstruction of the reciprocal space from the electron diffraction (ED) patterns evidences an orthorhombic distortion of the cell with regard to the ideal tetragonal cell of the $n = 1$ member of the RP series. The cell parameters are $a \approx 5.3$ Å $\approx a_p\sqrt{2}$, $b \approx 11.9$ Å $\approx 2(a_p + 1/2a_{RS})$, and $c \approx 5.3$ Å $\approx a_p\sqrt{2}$ (where a_p and a_{RS} are the parameters of the ideal perovskite and rock-salt-type structures, respectively). The conventional setting of the cell ($b > a > c$) has been retained since the perovskite layer of the structure is parallel to (010) and $a > c$, as in the calcium-rich $Ln_{1-x}Ca_xMnO_3$ perovskite exhibiting CO phenomena. The conditions of reflection at room temperature, hkl: $h + k = 2n$, $hk0$: $h = 2n$, $h0l$: $l = 2n$, are consistent with *Cmca* and C2cb as possible space groups. These conditions are illustrated in Figure 1a, b, and c, which present the [001], [010], and [100] ED patterns, respectively. The *Cmca* space group was chosen for the structure refinements.

On the basis of these observations, the cell parameters were refined to $a = 5.3025$ Å, $b = 11.8934$ Å, and $c = 5.2995$ Å from X-ray diffraction (XRD) and neutron powder diffraction (NPD) patterns (Table 1). The HREM study of "perfect" crystals allows the structural model of this phase to be confirmed, as shown in the image taken along the [101] zone axis direction (Figure 2). This viewing direction, which corresponds to the $\{100\}_p$ orientation of the perovskite layers and $\{110\}_{RS}$ of the rock-salt-type layers, is the most suitable for imaging the stacking sequence and identifying the different members. The experimental contrast is actually characteristic of an $n = 1$ member: the double rows of staggered bright dots (small black arrows) are associated to the double $[(Ca, Pr)O]_\infty$ layers and the single row of less bright dots to the $[MnO_2]_\infty$ layer. These slices are ≈6 Å thick and are alternately translated by $a_p/2$ along [101]. The ideal structure of this $n = 1$ member, built up from the intergrowth of one $[(Pr, Ca)MnO_3]_\infty$ perovskite layer and one $[(Pr, Ca)O]_\infty$ rock-salt layer, is given in Figure 2b.

Table 2. Interatomic Distances (Å) and Angles (°) in $Ca_{1.75}Pr_{0.25}MnO_4$

Mn−O(1)	1.940 (2) ×2	O1−Mn−O2	88.9 (4)
Mn−O(2)	1.8740 (1) ×4	O2−Mn−O2	89.970 (1)
		Mn−O2−Mn	179.8 (5)
		Mn−O1−Mn	179.97 (2)

Table 3. Thermal Factors (Å^2)

Isotropic Thermal Factors

Ca/Pr	Mn	O(1)
0.80 (4)	0.37 (4)	0.86 (3)

Anisotropic Thermal Factors for O(2)

β_{11}	β_{22}	β_{33}	β_{12}	β_{13}	β_{23}	Beq
99.8 (28.1)	20.1 (1.4)	167.7 (28.5)	0	−78.7 (6.3)	0	1.38

The NPD pattern registered on the 3T2 high-resolution diffractometer (Figure 2c) was then used to refine the structure in the *Cmca* space group. Refinements of the isotropic thermal factors led to rather high values for oxygen atoms (O2) in MnO layers ($B = 1.45$ Å^2) with $R_{bragg} = 6.31\%$. The oxygen deficiency was thus tested but did not allow the refinement to be improved. The oxygen sites were found fully occupied: the O(1) [site 8f: $(0, y \approx 0.16, z \approx 0)$] and the O(2) [site 8e: $(1/4, y \approx 0, 1/4)$] occupancy factors were found to be 1.018 (5) and 1.016 (6), respectively. Final refinements were carried out with an oxygen occupancy equal to 1. To understand this relatively high O(2) thermal agitation factor, we have chosen to refine the data with anisotropic thermal factors for O(2). Refined lattice parameters, atomic coordinates, and selected distances and angles are given in Tables 1 and 2, respectively. The thermal parameters are listed in Table 3. Diagonalizing the O(2) anisotropic temperature factors reveals a slightly elongated ellipsoid in a direction almost normal to the Mn−O vector. A plot of the final calculated and observed profiles is shown Figure 2c corresponding to $R_{bragg} = 5.04\%$. Although this R_{bragg} factor has been improved by this anisotropic refinement, its value remains relatively high. This result could indicate a dynamical disorder in the (010) plane, but the existence of twinning phenomena and static defects, evidenced by the electron microscopy study (next section), could also enhance this effect.

From Table 2 we clearly see that the MnO_6 octahedra are slightly elongated along the *b* axis; the Mn−O(1) bond (1.94 Å) is much longer than the Mn−O(2) distance (1.87 Å). The resulting Mn−O bond lengths of 1.87 Å (four equatorial distances) and 1.94 Å (two apical distances) are at the origin of a small gap between the Jahn−Teller split Mn e_g bands ($d_{x^2-y^2}$ and d_{z^2}). The Mn−O(2)−Mn angle in the basal plane very close to 180° implies no rotation of the MnO_6 octahedra.

Thus, this coupled HREM/NPD study shows that $Pr_{0.25}Ca_{1.75}$-MnO_4 exhibits a classical K_2NiF_4-type structure which consists of the intergrowth of single $[(Pr, Ca)MnO_3]_\infty$ perovskite layers with $[(Pr, Ca)O]_\infty$ rock-salt layers, without any ordering of Pr^{3+} and Ca^{2+} cations. The decoupling between the $[AMnO_3]_\infty$ layers along *b* avoids the octahedra tilting as in 3D manganites.

Detailed HREM Study Microstructural State. In fact, the ED investigation reveals that the microstructural state is, by far, more complex. For example, viewing the crystals along [010] shows the presence of weak reflections, which violate the aforementioned conditions of reflection of the *Cmca* space group (see white arrows in Figure 1b). Moreover, viewing along certain specific directions perpendicular to the *c** axis, diffuse streaks are systematically detected (see white arrows

(13) Rodriguez-Carjaval, J. *Physica B* **1993**, *192*, 55.

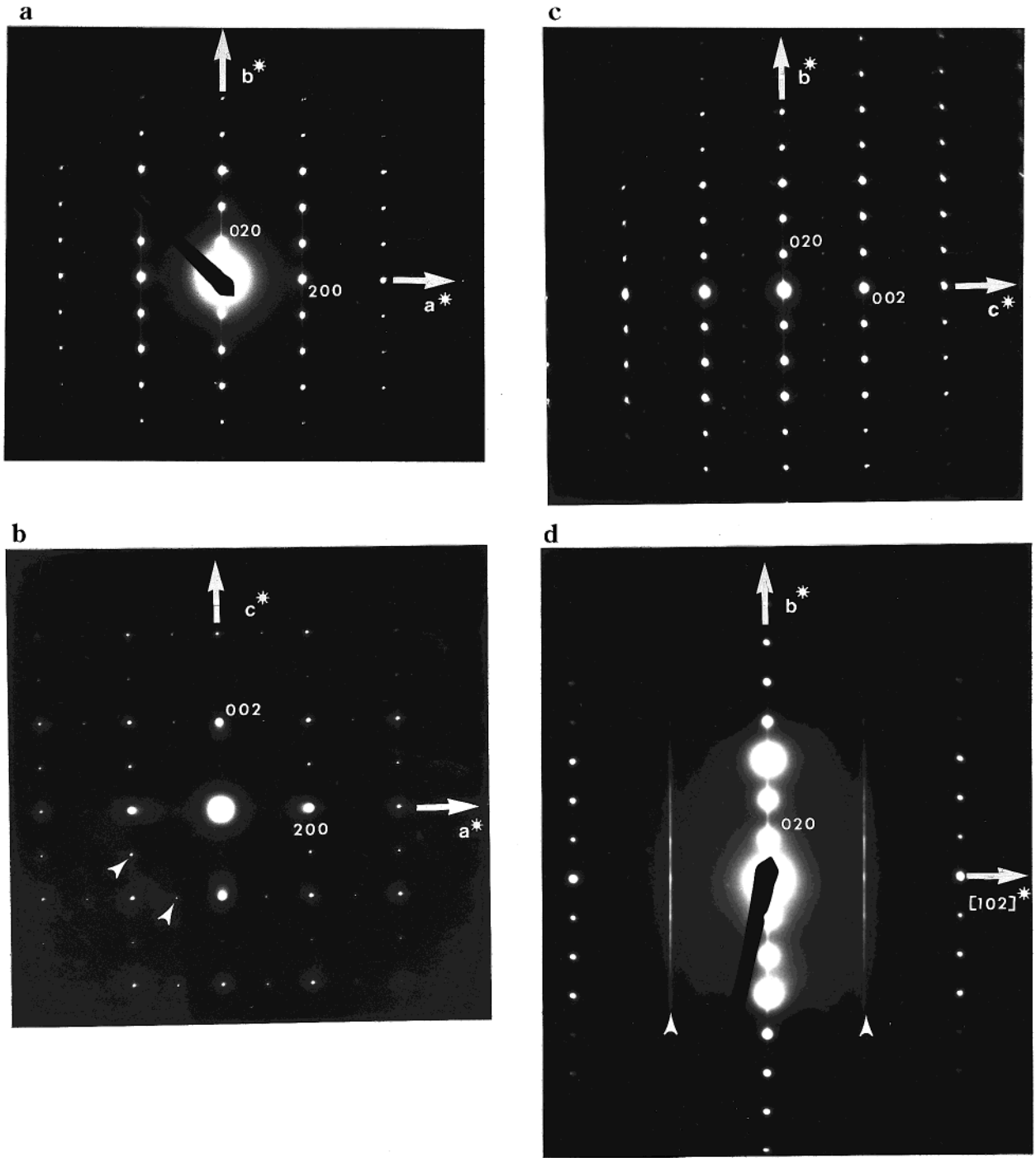

Figure 1. ED patterns of $Pr_{0.25}Ca_{1.75}MnO_4$: (a) [001], (b) [010], (c) [100], and (d) diffuse streaks are clearly visible in the [$\bar{2}$01] pattern.

in Figure 1d). They are the result of dynamical effects, microtwinning, local distortion, and disordering in the layer stacking.

(i) Microtwinning Domains. Because of their very close values, the *a* and *c* parameters (parallel to the {110}p directions of the tetragonal subcell) can be inverted from one octahedral (010) layer to the next one. Microtwinning phenomena, which are partly responsible for the diffuse streaks observed along *b** in Figure 1d, appear as a result of the superposition of very thin [$\bar{1}$02] and [$\bar{2}$01] oriented areas. This point was previously described and these domains, which are a few nanometers thick, imaged using dark field techniques for $Ca_{1.92}Pr_{0.08}MnO_4$;[12] they are not reproduced herein. In the [010] HREM images, this nanotwinning effect is scarcely visible. Image calculations confirm this observation, showing that the contrast of the [100] and [001] images are similar, whatever the focus value and crystal thickness. In some areas, however, the inversion of the $\vec{a}$ and $\vec{c}$ axes seems to be more easily detectable; in fact, as further detailed, we correlate this effect to the existence of areas which exhibit a lower symmetry. These complex phenomena can be linked to the supercell described in the Ca pure member Ca_2MnO_4.[14]

(ii) Layer Stacking Defects. A second type of defect also contributes to the appearance of diffuse streaks along $\vec{b}$*, suggesting the possible existence of layer stacking defects, which is a very common phenomenon observed in almost all the intergrowth structures. Usually in the RP's $[AO][AO_{3-\delta}]_m$, the defective members correspond to "infinite" perovskite slices, *m′* octahedra thick (*m′* is different from the nominal

(14) Leonowicz, M. E.; Poeppelmeier, K. R.; Longo, J. M. *J. Solid State Chem.* **1985**, *59*, 71.

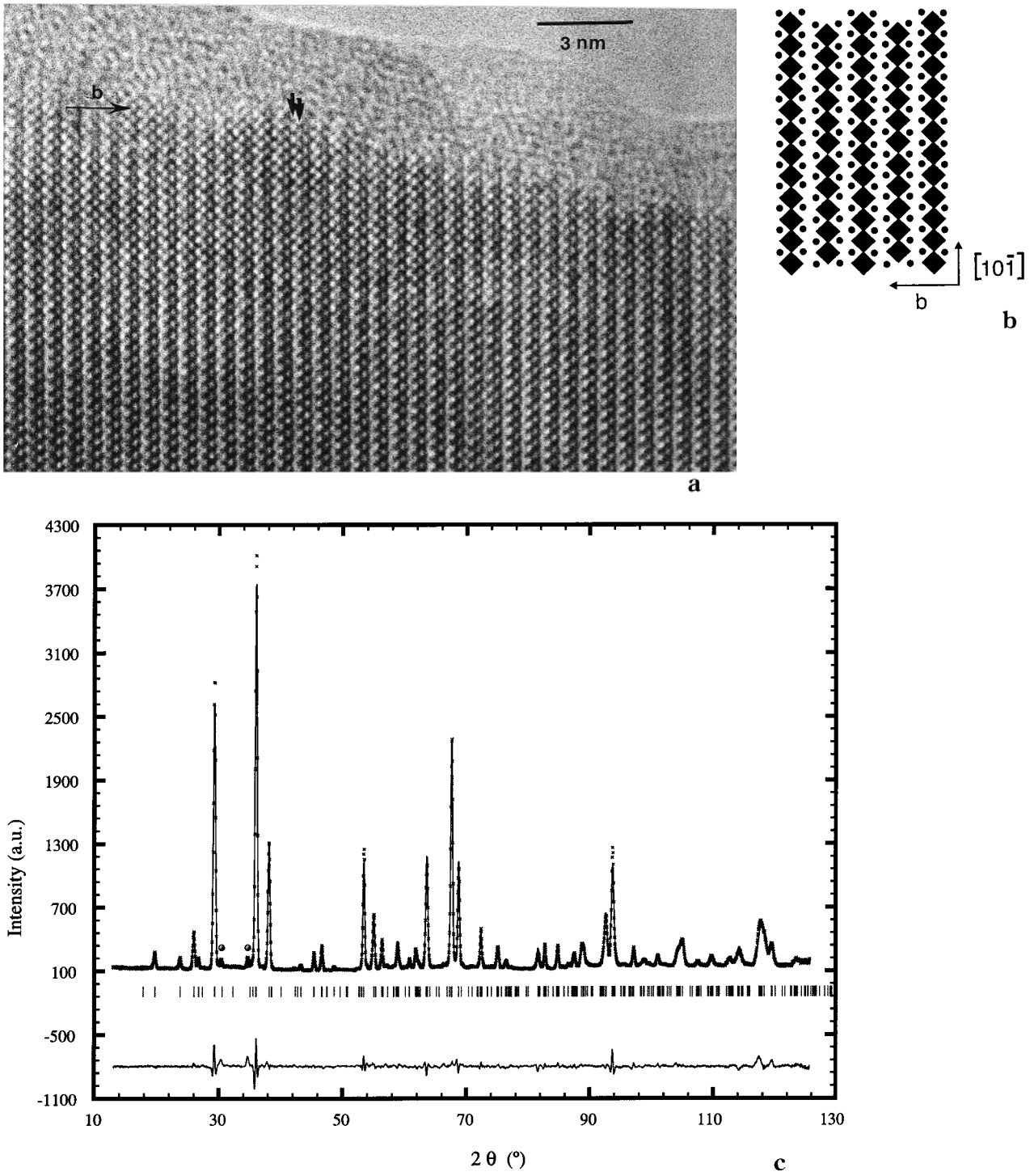

Figure 2. $Pr_{0.25}$ $Ca_{1.75}MnO_4$ structure: (a) [101] HREM image and (b) Idealized drawing of the $n = 1$ member of the RP series (dark circles = Ca and Pr atoms; the gray squares represent the MnO_6 octahedra). One rock-salt-type layer is built up from two adjacent "A−A" layers and one perovskite layer by two adjacent "AMn" layers. (c) NPD pattern registered on the 3T2 high-resolution diffractometer. Dots point two weak peaks not observed in the XRPD patterns. They do not vary with T and were not accounted for structure refinement.

composition m). The 2D character of the physical properties can be strongly modified by the presence of such defects, especially for high m' values. The probability of defect formation increases as m. In the $Ln_{2-y}Ae_yMn_2O_7$ manganites, several authors have reported the existence and role of such defects.[15]

The defects observed in the present material are not "infinite" defective perovskite slices; they run only over a few nanometers along the direction perpendicular to b (Figure 3) and exhibit a constant thickness. The neighboring regions present a highly disturbed contrast. This strong strain effect result in a so-called "pancake" aspect of the crystals, previously observed for $Ca_{1.92}Pr_{0.08}MnO_4$[12] and $Ln_{2-y}Ae_yMn_2O_7$.[16] The high-resolution images allow the structural mechanism to be understood. In the [100] image given in Figure 3, the double

(15) See, for example, MacChesney, J. B.; Potter, J. F.; Sherwood, R. C. *J. Appl. Phys.* **1969**, *40*, 1243. Seshadri, R.; Martin, C.; Maignan, A.; Hervieu, M.; Raveau, B.; Rao, C. N. R. *J. Mater. Chem.* **1996**, *6*, 1585. Battle, P. D.; Hepburn, J.; Millburn, J. E.; Rdaelli, P. G.; Rosseinsky, M. J.; Spring, L.E.; Vente, J. F. *Chem. Mater.* **1997**, *9*, 3215.

(16) Laffez, P.; Van Tendeloo, G.; Seshadri, R.; Hervieu, M.; Martin, C.; Maignan, A.; Raveau, B. *J. Appl. Phys.* **1996**, *80*, 5850.

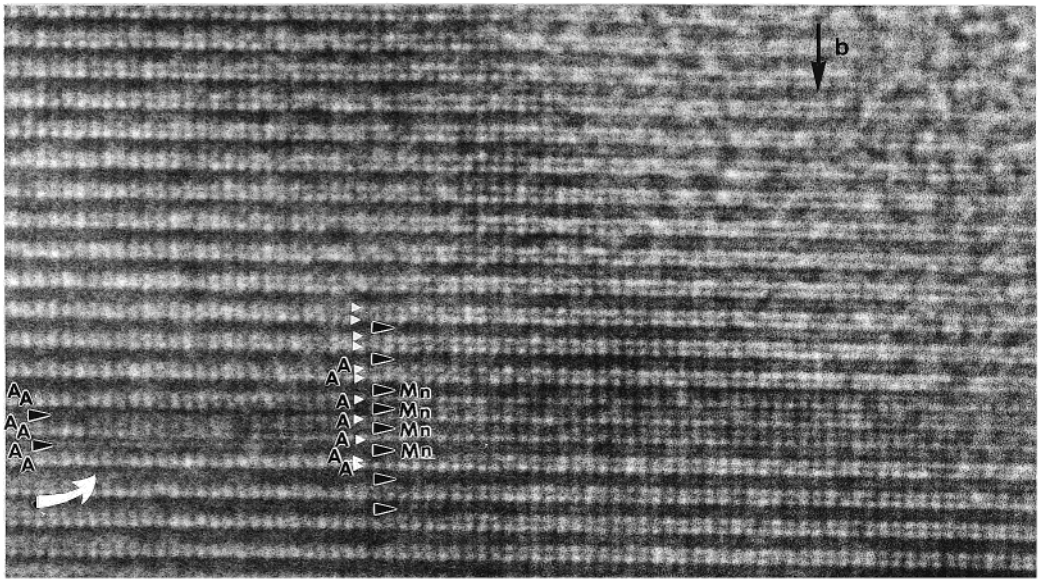

Figure 3. Pancakelike defect viewed along [100]. Note the cell distortion in the neighboring of the pancake. The stacking sequence of the [AO] and [MnO_2] layers is described by the cations, "A" and "Mn".

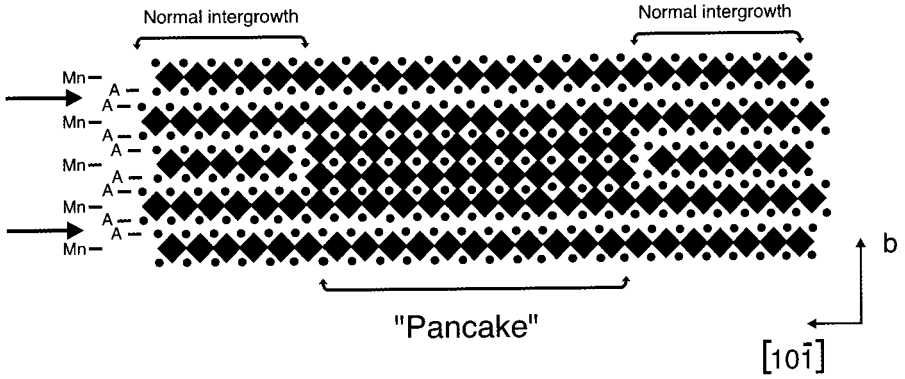

Figure 4. Idealized drawing of the defect, projected along [101]. In the left part, the sequence of the "A" and "Mn" layers is that of the regular structure.

rows of bright dots are associated to the double $[AO]_\infty$ layers (indicated by a small white arrow) and the $[MnO_2]_\infty$ layers are imaged as the darker rows (black arrows). The regular cation stacking along $\vec{b}$ [− −Mn−AA−Mn−AA−Mn−AA−Mn−AA−Mn−AA− −] is locally replaced by the sequence [− − Mn−AA−Mn−A−Mn−A−Mn−AA− −] at the level of the defect. This implies that the $[AO]_\infty$ and $[MnO_2]_\infty$ layers are interrupted at the level of the defect and connected to $[MnO_2]_\infty$ and $[AO]_\infty$ ribbons, respectively (Figure 4). This defect can be described as the introduction of a parallelepiped-shaped perovskite-type domain ("pancake") into the $Pr_{0.25}Ca_{1.75}MnO_4$ matrix. The pancakes are four octahedra thick along $\vec{b}$ and run over 5 to 10 nm, that is, about 30 to 100 octahedra along the [101] and [10$\bar{1}$] directions (Figure 4). It is remarkable that the thickness of the "pancake" is always close to 12 Å, that is, corresponds to the $b/2$ periodicity of a n = four members of the RP series $(Ln, Ca)_{n+1}Mn_nO_{3n+1}$, never to another one. This is easily explained by the fact that the b parameter of the matrix ($n = 1$) is also close to this value, which allows then a connection of the different layers along b.

Although this mode of connection of the different types of layers is the most suitable to decrease the strain effects in the "pancake" defect, a local distortion of the cell is, however, systematically detected in their close neighboring. This distortion explains the drastic contrast observed in the dark field images. The through focus series show that the symmetry lowering mainly affects the contrast of the oxygen positions, so that this phenomenon could be correlated to a local distortion of the framework to accommodate inner pancakes.

Charge Ordering at Low Temperature. Influence upon Magnetic and Transport Properties. The electron diffraction study of $Pr_{0.25}Ca_{1.75}MnO_4$ at low temperature (92 K) evidences weak superlattice reflections, appearing close to the main diffraction spots of the orthorhombic RT structure. These additional reflections occur along c^*, in incommensurate positions, leading to a supercell with $a \approx 5.3$ Å $\approx a_p\sqrt{2}$, $b \approx 11.9$ Å, $c \approx 1/q\ a_p\sqrt{2}$. Characterizing more than thirty crystallites, the average q value was determined to be close to 0.28. The second-order satellites are very weak (Figure 5). The reconstruction of the reciprocal space was carried out by tilting around b^* and c^*. Three ED patterns, [010], [100], and [110], recorded at 92 K are shown in Figure 5. Using a notation based on four indices $hklm$, the conditions of reflection are $hklm$: $h + k = 2n\ \forall\ l$ and m, $hk0$: $h = 2n$ ($k = 2n$) and $0klm$:l $= 2n$ ($k = 2n$) $m = 2n$, involving $Cmca(00\gamma)s00$ as the superspace group. The satellites are not visible in the [100] ED patterns (Figure 5b) because of the condition $m = 2$ and the weakness of the second-order satellites. These conditions provide two pieces of important information: first, the existence of a (m/s) antiphase modulation mirror and, second, the absence of a shift of the origin of the q wave along the b axis in neighboring perovskite layers. These satellites are similar to those observed in the ED patterns of the charge-ordered 3D perovskites $Ln_{1-x}Ca_xMnO_3$[17−27] and $La_{0.5}Sr_{1.5}MnO_4$.[8]

(17) Raveau, B.; Hervieu, M.; Maignan, A.; Martin, C. *J. Mater. Chem.* **2000**, *10*, 1.

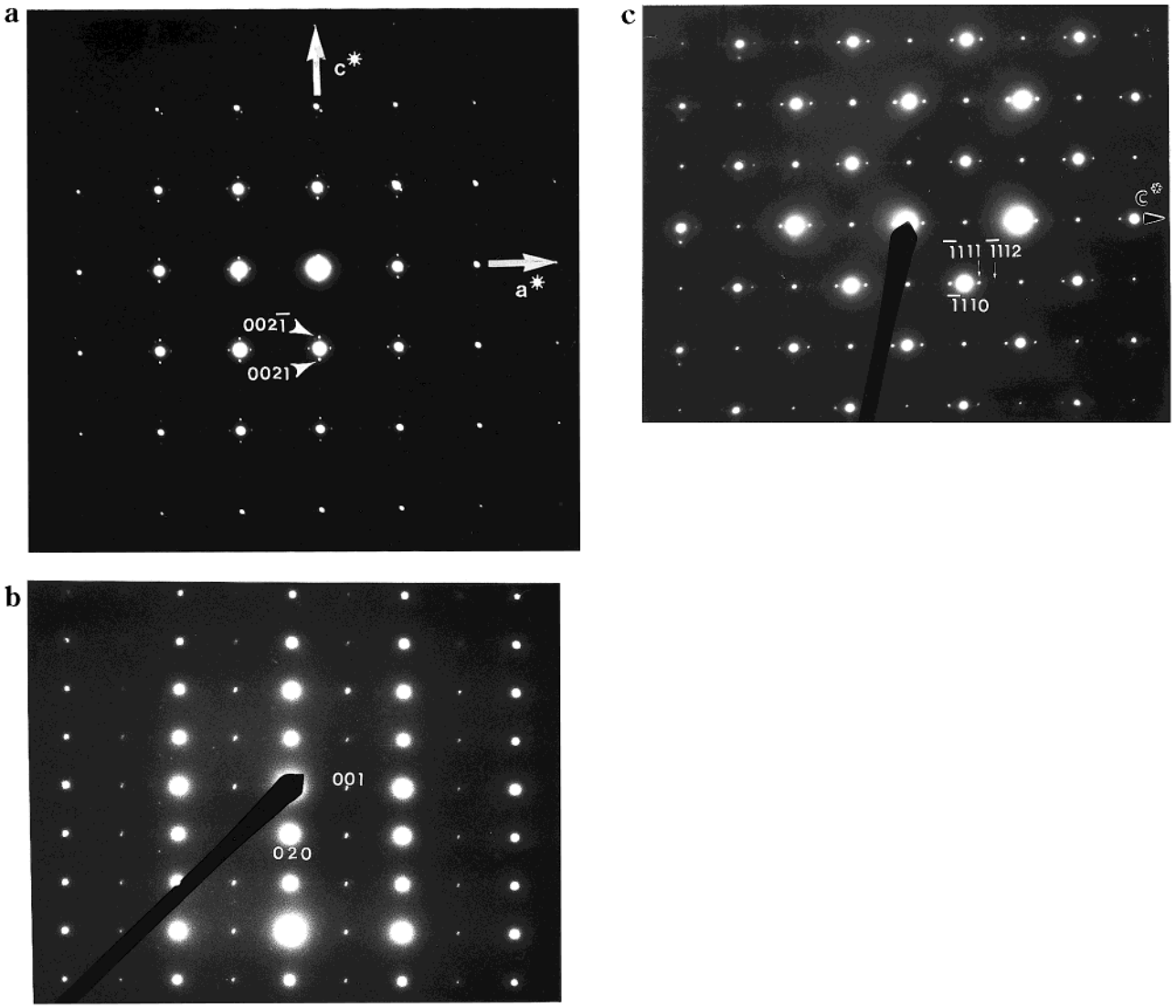

Figure 5. (a) [010], (b) [100], and (c) [110] ED patterns recorded at 92 K.

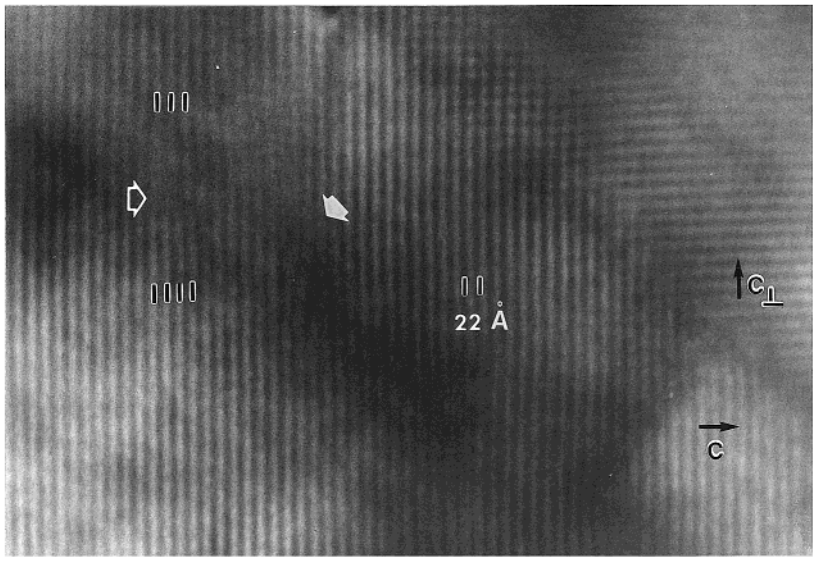

Figure 6. [010] lattice image showing the system of fringes at 92 K, oriented at 90°.

The [010] lattice image recorded at low temperature (T = 92 K) is given in Figure 6. A system of fringes, where one bright fringe alternates with one gray fringe along c, is established throughout the whole crystal. These fringes are

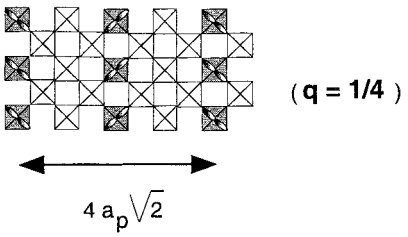

Figure 7. Example of the "**1**−**3**" manganese ordering, proposed for a 3D perovskite $Ln_{0.25}Ca_{0.75}MnO_3$.

regularly distributed, with an average interfringe distance close to 22 Å (4 $a_p\sqrt{2}$). Local variations of the periodicity are observed, correlated to the incommensurate q value; they are accommodated through dislocation-like mechanisms. Two examples of such variations are shown in Figure 6, where the large white arrows indicate the dislocations and the small vertical marks enhance the periodicity variation. In certain areas, two systems of fringes oriented at 90° (the two domains are pointed by the axes c and $c_\perp$) are observed in the lattice images. These observations are consistent with the existence of twinning domains observed at room temperature. In the present example, twinning boundaries are roughly parallel to $[\bar{1}01]_o$ and $[101]_o$ of the orthorhombic cell, that is, to$\{100\}_p$.

The important point deals with the amplitude of the modulation vector along c^*, namely $q = 0.28$, which is fundamentally different from that observed for another $n = 1$ member of the RP series, $La_{0.5}Sr_{1.5}MnO_4$ ($q = 0.50$). It is also different from that observed in $La_{1.2}Sr_{1.8}Mn_2O_7$,[28] an $n = 2$ member. Neutron scattering measurements showed incommensurate peaks characterized by a wave vector ($\pm\epsilon$, 0, ±1) with $\epsilon = 0.3$, but in this case, the modulation vector is rotated by 45° (i.e., parallel to a_p). The amplitude of the modulation vector could be correlated to the Mn^{3+}/Mn^{4+} ratio and, consequently, to charge- and orbital-ordering phenomena. In $La_{0.5}Sr_{1.5}MnO_4$, the Mn^{3+}/Mn^{4+} ratio is equal to 1, in agreement with a "**1**−**1**"-type ordering of the Mn^{3+} and Mn^{4+} rows along the [001] direction. In $La_{1.2}Sr_{1.8}Mn_2O_7$, the Mn^{3+}/Mn^{4+} ratio is equal to 1/2; the q value (0.3) is close to the theoretical value of a **"1**−**2"**-type ordering.

In $Pr_{0.25}Ca_{1.75}MnO_4$, the Mn^{3+}/Mn^{4+} is equal to 1/4, suggesting a "**1**−**3**"-type ordering of Mn^{3+}/Mn^{4+} rows with a $4a_p\sqrt{2}$ periodicity along c, (commensurate value: $q = 1/4$). Thus, referring to the models proposed for the Mn^{4+} rich perovskite, the ideal structure of the octahedral layer in the 3D $Pr_{0.25}Ca_{0.75}MnO_3$ consists of the ordered stacking along $\vec{c}$ of Mn^{3+} and Mn^{4+} rows of octahedra in such a way that one Mn^{3+} row alternates with three Mn^{4+} rows (Figure 7). This study clearly evidences that the manganese valence plays a prominent role in the amplitude of the modulation vector. However, a slight deviation of the modulation vector ($q = 0.28$) exists with regard to the ideal value ($q = 0.25$). This phenomenon could be due to a small deviation of the matrix from the nominal composition, correlated with the existence of the pancakelike defects. Another effect could be due to the presence of the RS-type layers, which may well strain the perovskite layers they sandwich, and thus modify the modulated structure. Such a strain effect has been observed in the perovskites deposited in the form of thin films, depending on the nature of the substrate.[29−30]

The evolution of the q value versus temperature is shown in Figure 8. Below 280 K, a plateau corresponding to the maximum q value (0.28) is observed. Above this temperature, the q value decreases abruptly to become nonmeasurable. In a same way, close to T_{CO}, the intensity of the satellites abruptly goes down, and the sharp satellites are replaced by weak diffuse streaks around the main spots of the electron diffraction pattern.

The temperature of charge-orbital ordering (T_{CO}) deduced from this curve, $T_{CO} = 275$ K, is closely connected with the magnetic and transport properties of this oxide. The magnetization curve M(T) (inset Figure 9) shows a maximum at $T_{CO} = 275$ K, which was previously interpreted as a change of the sign of magnetic fluctuations below this temperature. Similarly, the resistivity curve $\rho(T)$ (Figure 9), registered in the absence of a magnetic field upon cooling (or warming) shows a change of slope around $T_{CO} = 275$ K, ρ increasing more rapidly as T decreases below 275 K. Such an increase of the resistivity below T_{CO} can be considered as reminiscent of the abrupt increase of resistivity observed at T_{CO} for 3D charge-ordered perovskite manganites.

The effect of a magnetic field (0−7 T) on the charge-ordering transition has been tested; no significant CMR effect has been detected.

Concluding Remarks

This study of $Pr_{0.25}Ca_{1.75}MnO_4$ shows the structural complexity of the Ca_2MnO_4-type manganites, $n = 1$ member of the RP series, and especially their ability to form perovskite domains within the K_2NiF_4-type matrix, in the form of pancakelike defects. Microtwinning is also a characteristic of these materials, in connection with their orthorhombic distortion, which seems to be intrinsic to the $Ca_{2-x}La_xMnO_4$ manganites.

The important point of this study concerns the evidence of "**1**−**3**" Mn^{3+}/Mn^{4+} charge ordering below 275 K in the 2D manganites $Ln_{2-x}Ca_xMnO_4$. Such an ordering, which corresponds to the regular alternation of one Mn^{3+} octahedral row with three Mn^{4+} rows along c, is probably coupled with an ordering of the d_z^2 orbitals of Mn^{3+}. Unfortunately, microtwinning and local distortions did not allow the structure refinement at low temperature from NPD data. The evolution of the q vector versus T is in perfect agreement with the $\rho(T)$

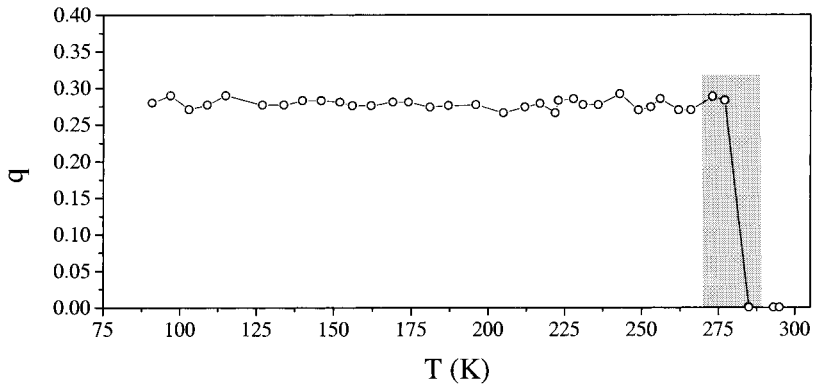

Figure 8. $Pr_{0.25}Ca_{1.75}MnO_4$: evolution of the q value versus temperature. In the plateau domain, the intensity of the satellites remains constant. Close to the T_{CO} (hatched zone), the intensity decreases abruptly, concomitantly with the q value, and the reflections exhibit diffuse streaks along c^*.

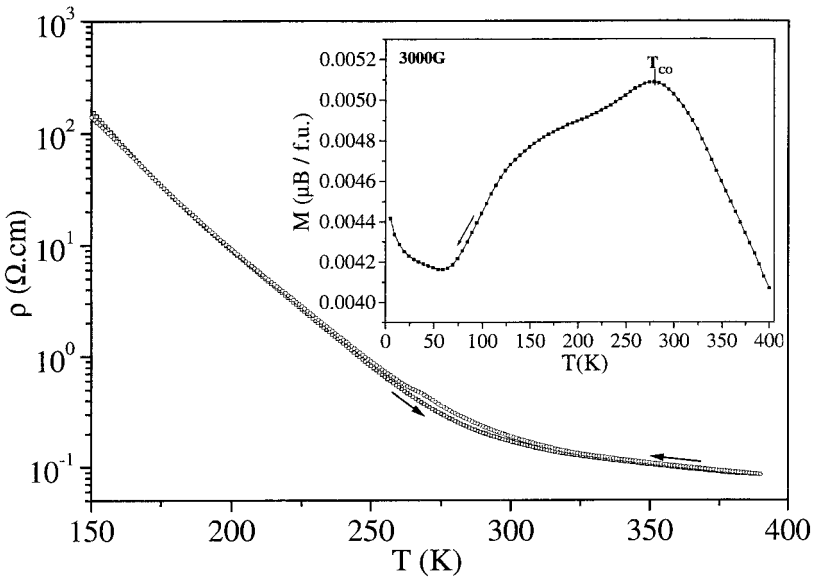

Figure 9. $Pr_{0.25}Ca_{1.75}MnO_4$: resistivity $\rho(T)$ and magnetization M(T) (inset) curves.

and M(T) curves, showing that the appearance of charge-orbital ordering induces both antiferromagnetic fluctuations and increase of resistivity. One important issue deals with the possibility to modify the q vector and T_{CO} by changing x in the series $Ln_{2-x}Ca_xMnO_4$ so that the magnetic and transport should be affected in a similar way. Investigations in this field are in progress together with efforts to produce defect-free samples.

Acknowledgment. The authors are grateful to C. Martin and A. Maignan for helpful discussions during this work and to G. André and F. Bourée for their neutron diffraction measurements and for their help.

CM010381V

(18) Tokura, Y.; Tomioka, Y.; Kuwahara, H.; Asamitsu, A.; Moritomo, Y.; Kasai, M. *J. Appl. Phys.* **1996**, *79*, 5288.
(19) Mahendiran, R.; Raychaudhuri, A. K.; Mahesh, R.; Gundakaram, R.; Rao, C. N. R. *J. Phys.: Condens. Matter* **1996**.
(20) Vogt, T.; Cheetham, A. K.; Mahendiran, R.; Raychaudhuri, A. K.; Mahesh, R.; Rao, C. N. R. *Phys. Rev. B* **1996**, *54*, 15 303.
(21) Caignaert, V.; Millange, F.; Hervieu, M.; Suard, M. E.; Raveau, B. *Solid State Commun.* **1996**, *99*, 173.
(22) Xiao, G.; Mcniff, E. J.; Gong, G. Q.; Gupta, A.; Canedy, C.; Sun, J. Z. *Phys. Rev. B* **1996**, *54*, 6073.
(23) Schiffer., P.; Ramirez, A. P.; Bao, W.; Cheong, S. W. *Phys. Rev. Lett.* **1995**, *75*, 3336.
(24) Lees, M. R.; Barret, J.; Balakrishnan, G.; Mack Paul, M.; Yethiraj, M. *Phys. Rev. B* **1995**, *52*, R14303.
(25) Tokunaga, M.; Miura, N; Tomioka, Y. *Phys. Rev. B.* **1998**, *57*, 5259.
(26) Barnabé, A.; Hervieu, M.; Martin, C.; Maignan, A.; Raveau, B. *J. Appl. Phys.* **1998**, *84* (*10*), 5506.
(27) Barnabé, A.; Maignan, A.; Hervieu, M.; Damay, F.; Martin, C.; Raveau, B. *Appl. Phys. Lett.* **1997**, *71*, 3907.
(28) Vasiliu-Doloc, L.; Rosenkranz, S.; Osborn, R.; Sinha, S. K.; Lynn, J. W.; Mesot, J.; Seeck, O. H.; Preosti, G.; Fedro, A. J.; Mitchell, J. F. *Phys. Rev. Lett.* **1999**, *83*, 4393.
(29) Haghiri-Gosnet, A. M.; Hervieu, M.; Simon, Ch.; Mercey, B.; Raveau, B. *J. Appl. Phys.* **2000**, *88*, N6, 3545.
(30) Mercey, B.; Hervieu, M.; Prellier, W.; Wolfman, J.; Simon, Ch.; Raveau, B. *Appl. Phys. Lett.* **2001**, *78*, 6612.